AIAA SciTech Forum
6-10 January 2020, Orlando, FL
AIAA Scitech 2020 Forum

10.2514/6.2020-1601

Realistic Guidance Performance during Lunar Rendezvous with Third Body Perturbation

Giordana Bucchioni* and Mario Innocenti †
University of Pisa, Department of Information Engineering, Pisa, Italy, 56122

Massimo Casasco‡
European Space Agency, European Space Research and Technology Centre, Noordwijk, The Netherlands, 2201 AZ

The paper describes the performance of a guidance law based on the Adjoint and SDRE methods in presence of reality representative models of sensors and actuators during the rendezvous phase of the proposed Heracles mission to the Moon. In recent years, the increased interest in returning to the Moon has motivated the necessity to develop accurate models for the analysis of missions that takes into account realistic system components. The paper reviews the mission's details, the rendezvous/berthing guidance algorithm with third body perturbation, and sensor's and actuators state of the art models. A Montecarlo analysis is used to validate the models in order to satisfy the safety of the trajectory. The results show that the proposed guidance and control are capable of maintaining safe relative motion between the vehicles.

I. Nomenclature

DOF	=	Degree Of Freedom
FOV	=	Field Of View
GNC	=	Guidance Navigation and Control
IMU	=	Inertial Measurement Unit
ISL	=	Inter Satellite Link
LAE	=	Lunar Ascent Element
LOP-G	=	Lunar Orbital Platform Gateway
LOS	=	Line of Sight
LVLH	=	Local Vertical Local Horizon
NAC	=	Narrow Angle Camera
NRHO	=	Near Rectilinear Halo Orbit
PID	=	Proportional Integral Derivative
PWM	=	Pulse Width Modulation
SDRE	=	State Dependent Riccati Equation
WAC	=	Wide Angle Camera

II. Introduction

In recent years international space agencies have considered returning to the Moon by building an orbiting space station called LOP-G [1] to explore our satellite and to facilitate future missions to Mars. A side mission named Heracles is in the planning stage to test technology's improvements in the field of autonomous operations and exploration by designing an autonomous lander. This mission was created initially as a collaboration between the European Space Agency (ESA), the Canadian Space Agency (CSA) and the Japanese Space Agency (JAXA) and it is composed by three phases: Landing, Exploring and Ascending. A Lunar Descent Module will land on the Moon surface and it will deploy a rover that would collect samples of the lunar terrain and load them to the Lunar Ascent Module (LAE).

*PhD candidate, Department of Information Engineering, University of Pisa, email: giordana.bucchioni@ing.unipi.it .
†Full Professor, Department of Information Engineering, University of Pisa, AIAA Associate Fellow, email: mario.innocenti@unipi.it .
‡Head, Guidance Navigation and Control Section, AIAA member massimo.casasco@esa.int .

The LAE module, then, will perform the ascent phase and a rendezvous/berthing procedure with the orbiting LOP-G. The focus of the paper is the rendezvous and berthing phase manoeuvre. The relative 6-DOF motion of the LAE with respect to the LOP-G is modelled under restricted three body problem hypothesis [2], the guidance strategy is selected and implemented and a realistic model of the LAE sensor/actuator equipment is used. The main aim of the paper is to present the sensor/actuators models and their influence on the performance of the GNC loop. The state of the art of sensor/actuator models is presented and discussed, the implemented models are shown, guidance and control algorithms are described, and an accurate Montecarlo analysis with variations of initial conditions is performed to show the behaviours of the selected guidance algorithm.

The measurement of the relative motion state variables during the rendezvous manoeuvre can be obtained following different approaches in the sense that such measurements can be execute on either vehicle. If performed on the target vehicle, the result would have to be transmitted to the chaser system, which may cause additional noise and could include the danger of link interruption. If performed on the chaser, the vehicle's relative position or velocity cannot be measured directly in the local-vertical local-horizon (LVLH). In this case the attitude of the sensor axes with respect to the local-vertical local-horizon (LVLH) frame of the target must be known with accuracy in order to resolve the actual range and direction measurements made in the chaser body frame into the needed values with respect to the target local-vertical local-horizon (LVLH).

One of the key-references in rendezvous literature [3] shows that during the close range rendezvous, direct accurate measurements of the relative target-chaser position, velocity, attitude and attitude-rate are necessary.

In particular, the following rendezvous navigation quantities are needed:

- Distance, range can be measured exploiting four different physical phenomena, triangulation, time of flight, phase shift or integration over time of a velocity measurement.
- Range-rate can be measured through Doppler shift effect or differentiation of the range measurements.
- The Line-of-sight Line of Sight (LOS) can be measured with a camera, or using two antennas or measuring a gimbal angle of a narrow beam signal either transmitted or reflected by the spacecraft.
- Relative attitude can be measured using the triangulation principle or using antennas, or using optical antennas.
- Angular rate can be measured thorough differentiation of the Line of Sight (LOS) and relative attitude or using gyroscopes and communication devices.

There are also additional sensors that may be especially useful during the rendezvous operations, for example those that measure motion variables and communications variables.

Once the necessary measurements are defined, different sensor suites can be selected, for example:

- Inertial Measurement Unit (IMU) (accelerometers and gyros), star trackers, Wide angle camera, Narrow angle camera, laser range finder.
- Gyroscopes, star trackers, cameras ([4] and [5]).
- Inertial Measurement Unit (IMU), star tracker, GPS and LIDAR ([6])
- Star tracker, Wide angle camera (Wide Angle Camera (WAC)), Narrow angle camera (Narrow Angle Camera (NAC)), RV LIDAR or multispectral camera [7].

Note that depending on the sensors used the accuracy of the measurements could be different.

Following [4] and [5], a general behavioural sensor model is given by:

$$x_m(t) = T_x(I + k)x(t - \tau) + b_x(t - \tau) + n_x(t - \tau) \tag{1}$$

Where: T is the misalignment, k is a scale-factor, b_x the bias, n_x stochastic noise and the delays are given by τ. In general, d_x, n_x and τ may not be constant in time and space. The model can be simplified removing the negligible parts, improving its understanding and the code execution time.

The actuator set is defined by the nature of the mission as well as the actuator distribution, but some critical non idealities were included in the models, in order to improve the models themselves. The main quantities that were modelled are the fluctuations of the thrust around its nominal value, the thrust misalignment and possible delays.

It is also important to select an appropriate method to allocate the the controlled forces and torques on the single thruster. Control allocation is an area widely studied and many algorithmic techniques exist, spanning from structural geometry approaches, to several types of optimisation methods. A survey of the most important control allocation techniques is presented in [8], for instance. Limiting ourselves to linear control allocation, the most common technique is the pseudo inverse. This approach, however, may not be efficient in case of control saturation, so alternatives can be found in the literature [8] such as: redistributed pseudo inverse and daisy chaining, direct allocation, error minimisation using linear programming and linear minimisation using quadratic programming.

In the same reference, some approaches are suggested that appear particularly suitable for spacecraft control allocation

problems. Additional references on the subject are: [9], [10], [11], [12] and [13].
The sensor and actuator's models are described herein, in addition to the reference frames, the rendezvous scenario, the equations of motion and the guidance algorithm. Sensors and actuators models are provided with their numerical values and then results based on Montecarlo simulations are presented.

III. Coordinate Systems Definition

The main coordinates systems used throughout the paper are now defined, and the relative notation is introduced.

A. Inertial Frame $\mathcal{I}$

The generic *inertial frame* centred in O and with unit vectors $\hat{I}$, $\hat{J}$, and $\hat{K}$, will be denoted as follows and it is not referred to any particular inertial or quasi-inertial location.

$$\mathcal{I}: \ \left\{O; \hat{I}, \hat{J}, \hat{K}\right\} \tag{2}$$

B. Three-Body Rotating Reference Frames

Consider two primary bodies, with masses M_1 and M_2, orbiting around their composite center of mass C in a collinear formation. A convenient frame for describing the motion of spacecraft in such a system is the *synodic reference frame*. It can be centered in one of the primaries center of mass, as in [14], and the unit vectors are defined as follows:

- $\hat{i}_s = -r_{12}/\|r_{12}\|$ where r_{12} is the position of M_2 with respect to M_1;
- $\hat{k}_s$ is perpendicular to the plane where the primaries revolve, and is positive in the direction of the system angular velocity vector;
- $\hat{j}_s = \hat{k}_s \times \hat{i}_s$ completes the right-handed coordinate systems.

This choice may be convenient when spacecraft measurements are taken with respect to the nearest primary. For instance in [14], the Sun-Earth/Moon system is considered, and the synodic frame is cantered on the Earth, since the spacecraft receives measurements with respect to it. In the following, we will refer to such a coordinate system as *primary-centred rotating frame*, and it will be denoted as

$$\mathcal{M}_i: \ \left\{O_i; \hat{i}_m, \hat{j}_m, \hat{k}_m\right\} \tag{3}$$

Where i is the index of the primary chosen for placing the coordinate frame. Fig. 1 shows the primary-centered rotating frame, centered on M_2 and the orbital frame (or Local-Vertical Local Horizon Frame).

C. The Local-Vertical Local-Horizon Frame

Rendezvous trajectories are generally described in a frame local to the target. This eases the analysis and the trajectory monitoring of incoming vehicles, as well as the definition of keep-out zones and admissible approaching corridors. The local-vertical local-horizon (LVLH) frame is usually employed for rendezvous scenario analysis,

$$\mathcal{L}_i: \ \left\{r_{it}; \hat{i}, \hat{j}, \hat{k}\right\} \tag{4}$$

and it is defined with respect to the primary body around which the target is orbiting. Denoting with r_{it} the target position with respect to the primary i, with $\left[\dot{r}_{it}\right]_{\mathcal{M}_i}$ the target velocity as seen from the primary, and with $h_{it} = r_{it} \times \left[\dot{r}_{it}\right]_{\mathcal{M}_i}$ the target *specific angular momentum* with respect to the primary, the LVLH frame unit vectors are defined and named as follows,

- $\hat{k} = -r_{it}/\|r_{it}\|$ points to the primary and is called *R-bar*;
- $\hat{j} = -h_{it}/\|h_{it}\|$, is perpendicular to the target instantaneous orbital plane and is called *H-bar*;
- $\hat{i} = \hat{j} \times \hat{k}$ completes the right-handed reference frame, and is called *V-bar*.

The above definition of the LVLH frame is consistent with the one given in [3]. The LVLH frame for a target orbiting around M_2 is shown in Fig. 1.

D. Body Frames

The *body frame* is centred in centre of mass and with the unit vectors parallel to principal axes of inertia. They are defined as follow:

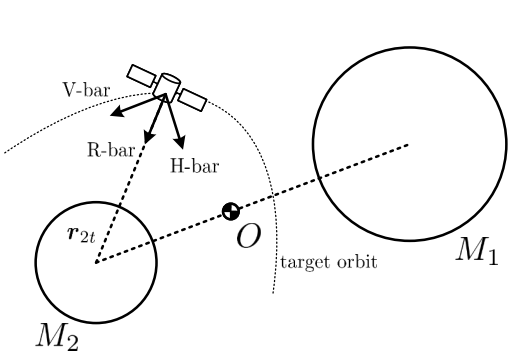

(a) Local-vertical local horizon frame $\mathcal{L}_2$.

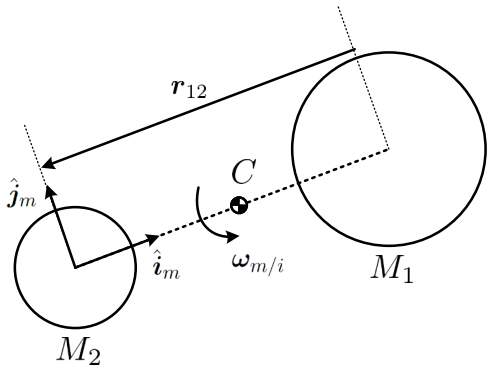

(b) Primary-centered rotating reference frame $\mathcal{M}_2$

Fig. 1 Coordinate Frames

$$\mathcal{T} : \left\{O_{t_{com}}; \hat{\mathbf{i}}_t, \hat{\mathbf{j}}_t, \hat{\mathbf{k}}_t\right\}, \quad \mathcal{C} : \left\{O_{c_{com}}; \hat{\mathbf{i}}_c, \hat{\mathbf{j}}_c, \hat{\mathbf{k}}_c\right\} \tag{5}$$

Which are respectively for target and chaser (See Fig. 2).

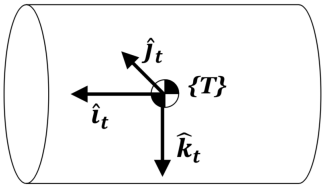

(a) Target body frame.

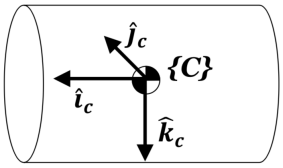

(b) Chaser body frame.

Fig. 2 Body Frames

E. Geometrical Reference Frame

In general, the definition of *Geometrical frame* is based on geometrical property of rigid body. We assume the vehicle described by an uniformly distributed regular cylindrical geometric form. We can define the *Geometrical frame* with the origin located on the geometrical centre of one of the chaser surfaces and the axes parallel to the principal axes of inertia.

$$\mathcal{G} : \left\{O_{t/c_{com}}; \hat{\mathbf{i}}_g, \hat{\mathbf{j}}_g, \hat{\mathbf{k}}_g\right\} \tag{6}$$

Fig 3 shows the geometrical frame of chaser, the geometrical frame of the target is described in a similar fashion. Other possible choices for the origin of the reference system could be either centred on the axis of the cone at $\frac{h}{2}$ (if we assume the cylinder height equal h) or in the principal engine of the spacecraft.

F. Docking Reference Frame

The *Docking frame* has the axes in same direction of the body frame. It is attached to the docking port structure and its origin is located at $\mathbf{r}_{p_{t/c}}$, the port position vector with respect to body frame.

$$\mathcal{D} : \left\{\mathbf{r}_{p_{t/c}}; \hat{\mathbf{i}}_d, \hat{\mathbf{j}}_d, \hat{\mathbf{k}}_d\right\} \tag{7}$$

In Fig. 4 we can see a general orientation of the docking frame.

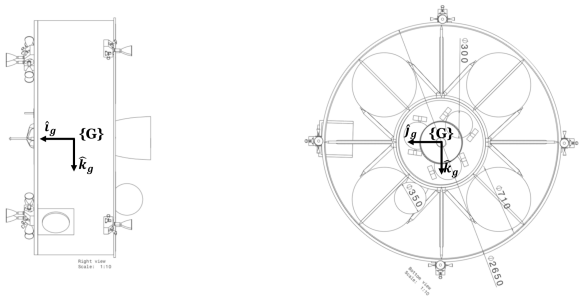

Fig. 3 Geometrical Frame for the Chaser

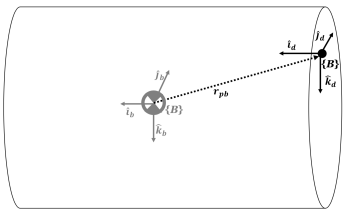

Fig. 4 Docking Frame

G. Sensor Reference Frame

The *Sensor frame* is directed along the main sensor's axis and its orientation depends on how the corresponding sensor is mounted on the vehicle, with origin located in $\mathbf{r}_S$, the sensor position vector with respect to the body frame. An example of sensor reference frame is shown in Fig. 5 for the camera's reference system.

$$\mathcal{S} : \left\{ \boldsymbol{r}_S ; \hat{\boldsymbol{i}}_S, \hat{\boldsymbol{j}}_S, \hat{\boldsymbol{k}}_S \right\} \tag{8}$$

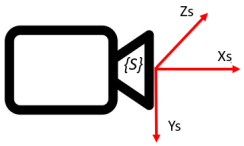

Fig. 5 Sensor Frame

IV. Mission scenario description

The paper main focus is the rendezvous phase of the mission. The two vehicles, LOP-G (target) and the LAE (chaser) must get arbitrarily close within specified constraints and no collision. The relative 6-DOF motion of the vehicles is modelled exploiting non inertial frames: LVLH, body , geometrical and port reference systems, The models are implemented under the Elliptical Restricted Three Body Problem hypothesis, in other words the two primaries are revolving with an elliptic motion around the common centre on mass and the third body is subject to the gravity influence of both the two primaries, Earth and Moon, in this case. The above dynamic evolution is considered accurate enough for guidance and control preliminary mission analysis.

The rendezvous manoeuvre is assumed to be composed by a sequence of four hold points, where an hold point is defined as a point at which the LAE chaser stops the relative approach to check its own status. At each hold point, the LAE guidance will evaluate if corrective manoeuvres are required, for instance in presence of failures that can compromise the mission's safety with the decision if it is safe to proceed with the rendezvous or it the necessary to abort the attempt.

In the sample scenario considered in the paper, the hold points are located along V-bar of the LVLH reference system [15] at the following distances between chaser and target berthing ports:

- Starting point: 50km.
- S1: 10km.
- S2: 1km
- S3: 100m
- S4: Berthing point.

For all the hold points the requirements are: zero relative velocity, zero relative angular velocity and an attitude that allows the target to be detected by the chaser's sensors. Both the target and chaser attitude initial conditions are non-zero. The duration of each phase are respectively: 3h, 2h, 2h and 2h. A qualitative propagation of the manoeuvre is shown in Fig. 6. The LOP-G station is assumed orbiting on a near rectilinear halo orbit (NRHO) around the Lagrangian point L2,

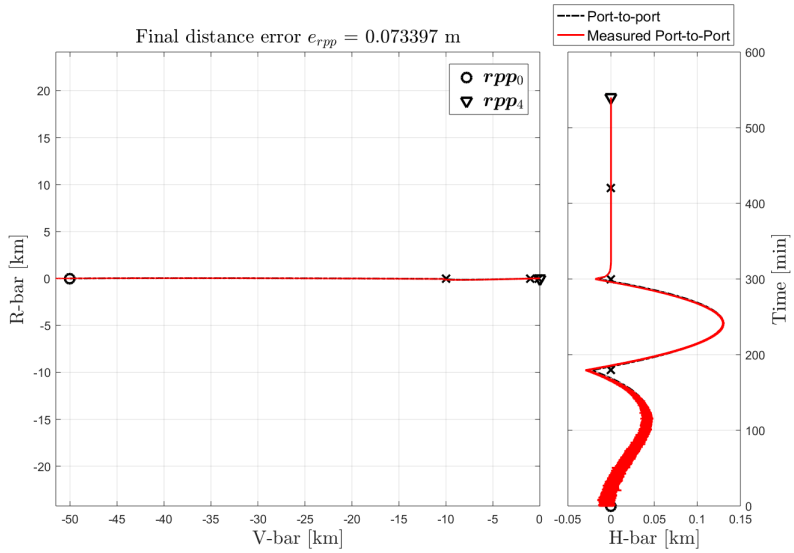

Fig. 6 Rendezvous Trajectory

defined as $\mathcal{M}_i$: $\{O_i; \hat{i}_m, \hat{j}_m, \hat{k}_m\}$ centred on the Moon, and it is considered to be a passive vehicle (Fig. 7).

The proposed guidance law to approach the LOP-G is composed by two different strategies, the details of which are shown in references [15] and [16]. In particular,

- The continuous trust manoeuvre is computed using the Adjoint method [15]. It is an open loop guidance that produces a double step force profile. This approach is used for relative distances larger that 1 km. The attitude is controlled with a PID controller that takes only local chaser attitude measurements with respect to an inertial reference system, and not relative attitude information.
- The State Dependent Riccati Equation (SDRE) controller [16] provides a computationally fast and preliminary optimal full state feedback nonlinear structure. The controller operates as a closed loop guidance used for relative distances below 1 km and it controls both the relative position and the relative attitude. The advantage of this approach for close distances is that it allows the inclusion of some constraints, such as berthing corridor approach and boundaries [3].

The guidance strategy must guarantee safety margins. In this paper, are considered safe all those final states that guarantee the margins shown in Table 1 [4]. The entire mission scenario was implemented in Matlab/Simulink environment within a software called ROSSONERO, developed at the University of Pisa.

V. Sensor models

The most commonly used rendezvous sensors and their models are described in the following sections.

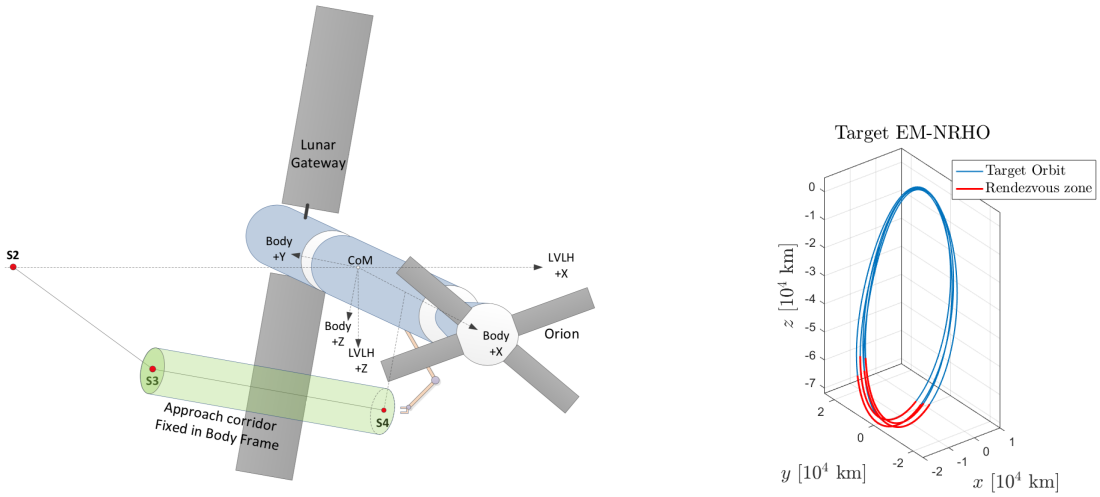

(a) LOP-G architecture

(b) Chaser body frame.

Fig. 7 Target orbit: NRHO L2

Table 1 Safety Margins

Relative Position errors < 0.1m.
Relative Velocity errors < 0.02 m/s.
Relative Attitude <5 deg
Relative angular rate < 0.15 deg/s

A. Gyroscopes

Gyroscopes are used to measure the angular rate of the body respect to an Inertial frame (typically measured in the sensor frame). According to the literature [4], [6] a generic gyroscope can be modelled as:

$$\bar{\Omega}^S_{B2I} = M_{SM}(\Omega^S_{B2I}) + b^S_\Omega + n^S_\Omega \tag{9}$$

where M_{SM} is a matrix containing scale factors and sensor misalignments. For gyroscopes, the noise is usually considered white. The bias (b_Ω), also called random walk rate bias, is not a static quantity but is driven by a second order Gaussian white noise process [17]:

$$\frac{d}{dt} b_\Omega = n_{\Omega b} \tag{10}$$

with,

$$E[n_{\Omega b}] = 0 \tag{11}$$

$$E[n_{\Omega b}\, n^T_{\Omega b}] = Q_b(t)\delta(t - t') \tag{12}$$

the two processes are assumed to be uncorrelated:

$$E[n_{\Omega b}\, n^T_\Omega] = 0 \tag{13}$$

B. Accelerometers

The accelerometers measure the spacecraft acceleration (typically measured in the sensor frame). The accelerometers are modelled as:

$$\bar{a}^S_B = M_{SM}(a^S_B) + b^S_a + n^S_a \tag{14}$$

Where M_{SM} is the matrix of scale factors and sensor misalignment. The accelerometer's noise is usually modelled as white noise and the bias is usually taken to be a constant [18].

C. Vision-based Measurement for Range, Line of Sight (LOS) and relative attitude

These sensors are used to measure the relative distance between the chaser and the target, the azimuth (β), the elevation angle (α) and the relative attitude at close distances (100-200m).
According to [4], it is possible to obtain range, Line of Sight (LOS) and attitude using a camera, and assuming that the noises (usually white) and biases (usually constant) are range-dependent. This behaviour can be modelled using Eq. (1), changing the noises and biases, as the range decrease. The range is divided into intervals and for each interval different noises and bias are defined. The intervals length depends on the number of pixels that the target occupies on the chaser's camera.
Cameras with different Field Of View (FOV) can be used during the approach manoeuvre, to improve the performance of the navigation chain. Analytically, the range R is described by:

$$\bar{R}(t) = R(t-\tau) + b_R(t-\tau) + n_R(t-\tau) \tag{15}$$

the Line of Sight is modelled for the elevation and azimuth by Eqs. (16) and (17) respectively:

$$\bar{\alpha} = \alpha(t-\tau) + b_\alpha(t-\tau) + n_\alpha(t-\tau) \tag{16}$$

$$\bar{\beta} = \beta(t-\tau) + b_\beta(t-\tau) + n_\beta(t-\tau) \tag{17}$$

Once R and Line of Sight (LOS) are known, it is possible to compute the target position in the sensor's frame (see Eqs. (15), (16) and (17)). The target-position components are explicitly calculated as:

$$\boldsymbol{\rho} = R \begin{bmatrix} \cos\alpha\cos\beta \\ \cos\alpha\sin\beta \\ \sin\alpha \end{bmatrix}$$

The Euler angles sequence (3,2,1) is given by:

$$\bar{\boldsymbol{\theta}}(t) = \boldsymbol{\theta}(t-\tau) + b_\theta(t-\tau) + n_\theta(t-\tau) \tag{18}$$

the attitude can also be expressed in quaternions, and it is usually available only at close distances.

D. Star Sensors

Star trackers determine the spacecraft inertial attitude with respect to an internal frame, during close relative navigation; they are not used as relative sensors for rendezvous, but are needed for absolute attitude determination. Their measure can be expressed in Euler angles using Eq. (18) or in quaternions (q_0, q_1, q_2, q_3), from 19.

$$\bar{q} = q \otimes q_{noise} + b_q \tag{19}$$

where q is the quaternion without noise, q_{noise} is the quaternion resulting from the sensor noise and b_q is a bias.
The $\otimes$ is the Kronecker product in Eq. (20):

$$p \otimes q = \begin{bmatrix} p_0q_0 - p_1q_1 - p_2q_2 - p_3q_3 \\ p_0q_1 + q_0p_1 + p_3q_2 - p_2q_3 \\ p_0q_2 + q_0p_2 + p_1q_3 - p_3q_1 \\ p_0q_3 + q_0p_3 + p_2q_1 - p_1q_2 \end{bmatrix} \tag{20}$$

E. Spacecraft-to-Spacecraft

Spacecraft relative range can be measured using a camera, as already discussed above, or exploiting the time of flight principle or the phase shift principle by an Inter Satellite Link (ISL) . In both cases the errors are nearly a linear function of the range. In some manoeuvre-phases, the range may be measured trough a laser range-finder as an alternative way, however the measure depends also on the relative attitude between chaser and target vehicles.

F. Spacecraft-to-Spacecraft Communication

As specified in the introduction, it might be necessary to have communications available between target and chaser (must if we envision the vehicles carry humans), this will introduce additional noise and delay through a general model given by:

$$\bar{x} = x(t - \tau) + b_x(R) + n_x \tag{21}$$

where x is the communicated measurement and n_x is the communication noise. It is possible to add additive random variables to simulate communication interrupt or errors.

VI. Actuator models

In general, the set of actuators implements the firing command sequences, it allows the vehicle to separate the motion along different axes, and the translational motion from the rotational one. With reference to similar missions, the actuator suite used in the present paper consists of 16 RCS-thrusters of 10N each, and is extensively described in [19]. They are positioned so to be able to control position and attitude separately and to be fault-robust within prescribed operational constraints. Moreover, the thrust should be sufficiently high to avoid saturation during the manoeuvre. The different sources of error used in our thruster model can be summarised in three main contributions:

- Thrust Magnitude Errors.
- Thrust Direction Errors.
- Rise/Fall time and delays.

A. Thrust Magnitude Model

The thrust magnitude model is given by:

$$\bar{F} = F \cdot \eta_{1BIT} \cdot (1 + \delta\eta_{1BIT}) \tag{22}$$

where F is the nominal thrust level at steady state, η_{1BIT} is the theoretical bit efficiency and $\delta\eta_{1BIT}$ is the impulse bit efficiency random variation. In our scenario, F is equal to 10N. The theoretical impulse bit efficiency is computed from the empirical formula (23), which is based on the duration of the thruster firing command (t_{on}) and the thruster off-time (t_{off}).

$$\eta_{1BIT} = exp\left(\frac{-c_1}{1000t_{on} + c_2/1000t_{off}}\right) \tag{23}$$

t_{on} and t_{off} are expressed in seconds and c_1 and c_2 are called efficiency factor constants. According to [20] t_{on} e t_{off} are selected using a Pulse Width Modulation (PWM) approach. The random variation of the impulse bit efficiency $\delta\eta_{1BIT}$ is assumed as Gaussian with zero mean and the standard deviation $\sigma_{\eta_{1BIT}}$ is given by:

$$\sigma_\eta = min(max(\sigma_{\eta_{min}}, \sigma_{\eta_{coef1}} \cdot (1000t_{on})^{sigma_{\eta_{coef2}}}), sigma_{\eta_{sat}}) \tag{24}$$

B. Thrust Direction Model

Thrust misalignment is mainly composed by two contributions: Internal and External.
The first direction error is due to a misalignment between thrust vector and flange. These errors are constant over a single thruster firing, but they change randomly from one firing to the next, so the internal uncertainty is assumed to behave as a Gaussian noise.
The external errors are due to possible misalignment between flange and master reference cube. These uncertainties remain constant for the entire simulation, but they change form a simulation to another. As a consequence, the external uncertainty is assumed to behave as a uniformly distributed random variable.

C. Additional Uncertainties

In addition to magnitude and direction uncertainty, it is necessary to take into account also the Rise/Fall time behaviours as well [4]. In this paper, the thrust will be discretized following a Pulse Width Modulation (PWM) logic. The motors have also a dynamic and minimum t_{on} and t_{off} times. The Rise/fall times are taken into account using a

filtering operation: The PWM signal is filtered by a 1^{st} or 2^{nd} order dynamics as shown in Eqs. (25) and (26). The filter equation can also include potential delays τ.

$$F_1 = \frac{A}{s+b} e^{-\tau} \tag{25}$$

$$F_2 = \frac{\omega_n^2 e^{-sT_{\Delta v}}}{s^2 + 2\zeta\omega_n s + \omega_n^2} e^{-\tau} \tag{26}$$

D. Control Allocation Approaches

In this paper, the control allocation algorithm extends the methodology presented in reference [9]. Details can be found in [21]. It avoids the use of a PWM module after the control allocation, because it computes the optimal combination of duty-cycle to minimise a linear cost function:

$$J = f^T F_s f = [1 \;\; 1 .... 1]^T \tag{27}$$

Another advantage is that, by minimising the duty-cycle, the fuel-consumption is also minimised since is proportional to the summation of all thrusters. The selected control allocation technique is combined with a static allocation map, to reduce the allocation time. In other words, the proposed allocation algorithm computes an off-line a static allocation maps that allocates the sub-optimal duty cycle combination, in the sense of duty cycle duration, at each PWM step.

VII. Sensor and actuator numerical properties

A. Sensors

In this section, the numerical characteristics of the selected sensor sets are listed, based on current information on the mission under study. In particular, the logical sequence of sensor usage is shown in Fig. 8, to cover the entire mission. The sensors modelled in this work are:

- Inter Satellite Link (ISL).
- Narrow Angle Camera (NAC): $FOV = 3°$, and detector 1024x1024 px.
- Wide Angle Camera (WAC): $FOV = 40°$, and detector 1024x1024 px.
- Star Tracker plus Inertial Measurement Unit (IMU).

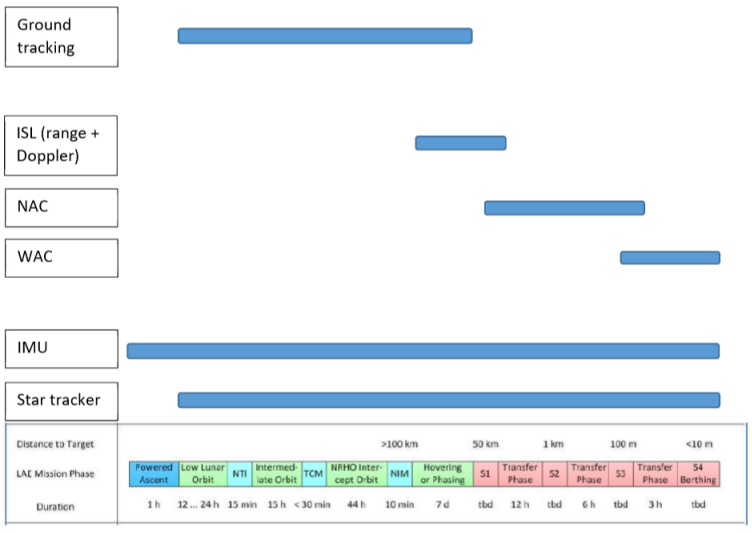

Fig. 8 Chaser Navigation Suite Concept

The numerical values of large-medium-and short ranges are defined as functions of the error entities and shown in Table 3.

Table 3 Sensor Data

Sensor	Uncertainty Param	Value	Range
ISL	b_{ISL}	3% R	all
NAC	b_{LOS}	100% error(1-2px)	long distances
	b_{LOS}	100% error(5-50px)	medium distances
	b_{LOS}	0.2% R	short distances
	b_R	2% R	
	b_θ	5°	
WAC	b_{LOS}	100% error(1-2px)	long distances
	b_{LOS}	100% error(5-50px)	medium distances
	b_{LOS}	0.2% R	short distances
	b_R	2% R	
	b_θ	5°	
STR + IMU	WN σ	5 arcsec	all

Starting from the error along the LOS it is possible to estimate the lateral displacement error as showed in Eq. (28), both the vertical position error and the horizontal one are computed using the same formula.

$$L_{bias} = 2 \cdot R \ \sin(0.5 \ FOV/res \cdot b_{LOS} \cdot \pi/180) \tag{28}$$

where res is the camera resolution, in other words the number pixels that compose the camera's sensor (1024 x1024, in this case).

NOTE: although the accelerometer is not explicitly implemented, its contribution is reflected in an actuation delay in the actuator's model and the the fact that Body-Frame and the Geometric-Frame are coincident at each instant.
Inter Satellite Link (ISL), Wide Angle Camera (WAC), Narrow Angle Camera (NAC) are implemented as a single block, and the appropriate sensor is selected in relation with the the relative distance between chaser and target, in particular the amount of error committed by the selected sensor's suite helps to define the working ranges of each set-up (short, medium and long distances). For clarity's sake, all the quantities are also depicted in Fig. 9.
If the relative distance is above 10 km, the distance is referred and long distance and the sensor used to estimate the range is the ISL, it has an error in range estimation equal to 3%R and from Fig. 11 it is possible to notice that the range estimation error produced by the NAC is above 3% for ranges longer than 6 km. The error shown in Fig. 11 is computed as:

$$b_R\% = 0.5\frac{ang_{px}}{2\alpha_1}100 \tag{29}$$

For the LOS (α and β) and consequently of the lateral displacements the Narrow Angle Camera is used and an error of 100% of the target angular visible size is taken into account (about 1-2px), at long distances.
At medium distances (10 km - 1 km) the Inter Satellite Link (ISL) is deactivated and the range is estimated using the NAC as:

$$b_R = \frac{l}{2}\left(\frac{\cos\alpha_c}{\tan\alpha_1} + \sin\alpha_c\right) \pm 0.5\frac{ang_{px}}{2\alpha_1} \tag{30}$$

where:

- l is the target visible area length, that is equal to 5m;
- α_c is the measured azimuth angle of the target centre of mass, affected by an error of 100% of the target illuminated size.
- α_1 is the difference between the azimuth of the centre of the illuminated zone and the azimuth of a side of the illuminated zone.
- ang_{px} the pixel angular size of the visible Target area.

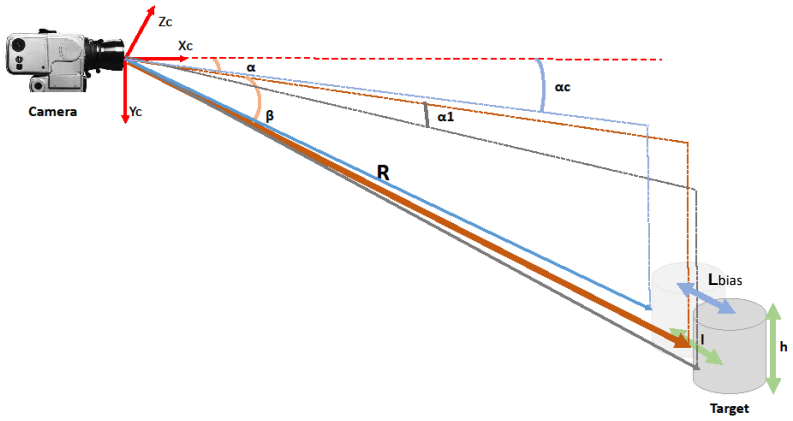

Fig. 9 Reference Quantities and Camera Frame

The LOS is still measured with the NAC, and its assumed error is between 5 to 100 px (100% of the target illuminated side). The LOS is computed using Eq. (31) and the trend is reported in Fig. 10. α_{err} defines the limits between medium distances and short distances, and are considered medium distances those for which $b_R\%$ is less than $3\%R$ but the lateral displacement error is less than 100px, as a result the medium distances are those included in the range 10 km-1 km.

$$\alpha_{err} = \arctan \frac{l}{R} \tag{31}$$

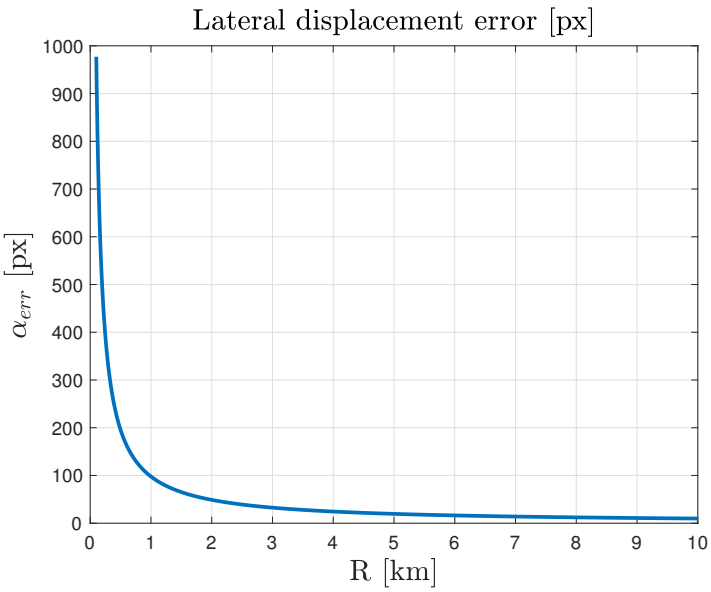

Fig. 10 Lateral Displacement Error

The short distances are those between 1 km and 5m, here the sensor used is the WAC, and the error on LOS as an error on the lateral displacement is equal to $0.2\%R$ and the bias error on R is $2\%R$. At short distances it is also possible to estimate the relative attitude, with a maximum error of 5 degrees per axis.
The estimation of the linear velocity is based on the differentiation principle and a subsequent Kalman filtering procedure, however, in this work, the entire navigation chain is modelled by Eq. (32).

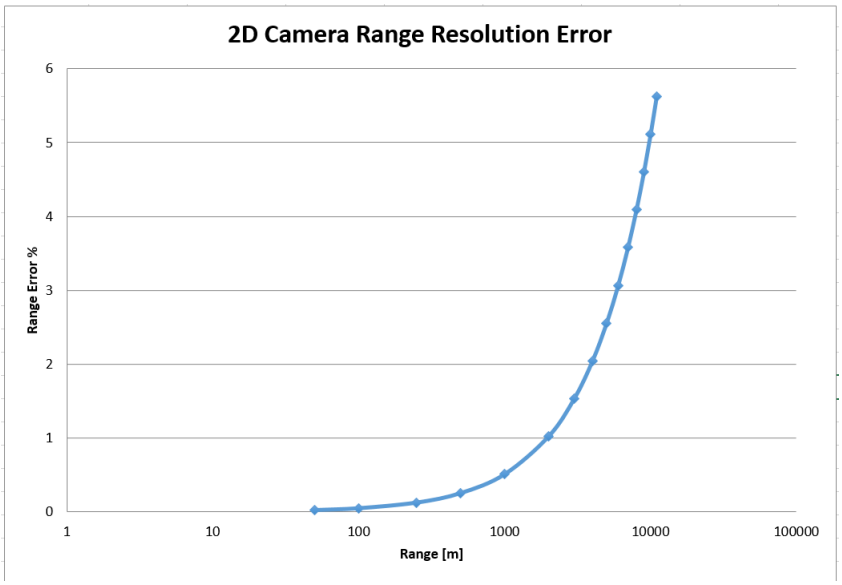

Fig. 11 Percent Range Error Estimate with NAC

$$\tilde{\dot{\rho}}_{pp} = \dot{\rho}_{pp} + \|\tilde{\rho}_{pp} - \rho_{pp}\| n_{\dot{\rho}_{pp}} \tag{32}$$

where $\tilde{\dot{\rho}}_{pp}$ is the relative port-to-port velocity affected by the error, $\dot{\rho}_{pp}$ is the velocity without errors, $\tilde{\rho}_{pp}$ is the relative position affected by error, ρ_{pp} is the relative position and $n_{\dot{\rho}_{pp}}$ is a white noise. A similar approach is used to model the angular velocity error, and shown in Eq. (33):

$$\tilde{\omega} = \omega + \|\tilde{\theta} - \theta\| n_{\omega} \tag{33}$$

$\tilde{\omega}$ is the relative angular velocity affected by the error, ω is the velocity without errors, $\tilde{\theta}$ is the relative attitude affected by error, θ is the relative attitude and n_{ω} is a white noise. It is important to remark that the range is measured with the camera, only when the the target is within the camera's FOV, the sensors are initialised at every hold point and the sensor's suite changes only at the hold points depending on the target-chaser distance. The range measures are always available because the implemented controllers are able to keep the target within the camera's FOV.

B. Actuators

The location of the thrusters depends on the vehicle, its configuration and geometry, and mission. In the following section, we will be briefly describe the actuators configuration and the contribution that each actuator gives to torques and forces that act on the chaser centre of mass in the body frame reference. The frame used to reference the actuators' location is the Geometrical frame shown in Fig. 3.

NOTE: the chaser vehicle is considered as a perfect cylinder with uniform density and constant mass, therefore, the body reference system $\mathcal{G}$ has been located along principal axes of inertia. The reference geometry data are:

- $r_1 = 2590/2\ mm$
- $h = 900\ mm$
- $r = \sqrt{r_1^2 + h^2}$
- $\alpha = \arctan(\frac{r_1}{h/2})$
- The smaller thrusters provide 10N of thrust, and they are depicted in Fig. 12. They provide fine control of a low mass (propellant thanks nearly empty) vehicle that will be grabbed by the target's robotic arm [7], following successful berthing. During the rendezvous phase, only the larger ones are used for both attitude and translational control. Fig. 12 shows the thruster configuration and numbering as well.

The projection of the thrust of each motor into torques and forces on the entire body are described in chaser body axes.

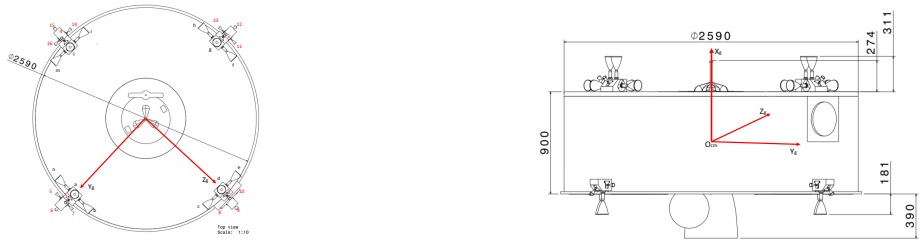

(a) up-view

(b) side-view.

Fig. 12 Chaser Engine Configuration

Table 5 Actuator Data

Actuator Parameter	Uncertainty Param	Value
Efficiency factor constant	c_1	7.6
	c_2	200
Random Impulse components	$\sigma_{\eta_c oef1}$	0.5356
	$\sigma_{\eta_c oef2}$	-0.8446
	$\sigma_{\eta_m in}$	0.01
	$\sigma_{\eta_s at}$	0.0766
Internal Thrust dir (Gaussian distr)	*mean*	0
	σ_I	0.1°
External Thrust dir (Uniform distr)	*mean*	0
	interval	$[-0.2°, 0.2°]$

Let F_s be the 16^{th}-dimensional vector that contains the thrust provided by the small thrusters:

$$F_s = \begin{bmatrix} F_1 & F_2 & F_3 & \dots & F_{14} & F_{15} & F_{16} \end{bmatrix}^T \tag{34}$$

The vector of forces and torques, in chaser body frame called τ and is defined as:

$$\tau = \begin{bmatrix} F_x & F_y & F_z & N_x & N_y & N_x \end{bmatrix}^T \tag{35}$$

The linear relation between τ and F_s is given by Eq. (36).

$$\tau = [B_s] \begin{bmatrix} F_s \end{bmatrix} \tag{36}$$

Where B_s is called control allocation matrix and it is defined in Eq. (37).

$$B_S = - \begin{bmatrix} C\beta & C\beta & C\beta & C\beta & 0 & -C\beta & 0 & 0 & -C\beta & 0 & 0 & -C\beta & 0 & 0 & -C\beta & 0 \\ S\beta & 0 & -S\beta & 0 & 0 & S\beta & 0 & -1 & 0 & 1 & 0 & -S\beta & 0 & -1 & 0 & 1 \\ 0 & S\beta & 0 & -S\beta & -1 & 0 & 1 & 0 & S\beta & 0 & 1 & 0 & -1 & 0 & -S\beta & 0 \\ 0 & 0 & 0 & 0 & -rS\alpha & 0 & rS\alpha & -rS\alpha & 0 & rS\alpha & rS\alpha & 0 & -rS\alpha & -rS\alpha & 0 & rS\alpha \\ 0 & -rS\beta\alpha & 0 & rS\beta\alpha & -rC\alpha & 0 & rC\alpha & 0 & rS\beta\alpha & 0 & -rC\alpha & 0 & rC\alpha & 0 & -rS\beta\alpha & 0 \\ rS\beta\alpha & 0 & -rS\beta\alpha & 0 & 0 & -rS\beta\alpha & 0 & -rC\alpha & 0 & rC\alpha & 0 & rS\beta\alpha & 0 & rC\alpha & 0 & -rC\alpha \end{bmatrix} \tag{37}$$

using the common trigonometric shorthand notation: $C\alpha = \cos\alpha$; $S\alpha = \sin\alpha$; $C\beta = \cos\beta$; $S\beta = \sin\beta$;$S\beta\alpha = \sin(\beta - \alpha)$.

The significant numerical values used in the paper are shown in Table 5.

VIII. Results

All models and the controllers were implemented in the ROSSONERO software [21], with the code written in Matlab/Simulink environments. An extensive Montecarlo analysis was carried out to evaluate the sensitivity in terms of final errors and energy consumption of the selected guidance profile, while guaranteeing the required safety margins. During the Montecarlo simulation the quantities were changed uniformly random criteria within the boundaries shown in Table 6.

The performance analysis approach consisted in selecting a target mission set-up and then changing, within a

Table 6 Sampling Intervals

Position interval	[-1km 1km]
Velocity Interval	[-10cm/s 10 cm/s].
Angle interval	[-5 deg; 5deg]
Angular Rate interval	[-0.5 des/s ; 0.5 deg/s]

uniform-random closed set, the initial conditions one by one (relative position, relative velocity, chaser attitude and chaser angular velocity with respect to the LVLH).

The results of the analysis are summarized in a set of five 4-D plots, shown in the next figures from 13a to -16j that represent the final errors and the ΔV consumption with respect to the changes in initial conditions, as well as the error's distributions.

A. Comments

Several considerations can be made from the evaluation of the simulation data.

- The 90% of position errors are less than 10 cm, except when the initial velocity is non non zero, in that case the percentage slightly decreases.
- The mean value of the final velocity error is around 2 mm/s in every case with a maximum deviation value around 8 mm/s.
- The attitude angles norm is less than 0.45 degrees in all cases.
- The maximum angular velocity error does not exceed 0.14 degree per second.
- The average energy consumption is around 35 m/s except in the case of non zero initial relative velocity, in that case, in fact, the energy consumption distribution has higher values. In the selected scenario, the target consumption is about 30 m/s. However, the energy consumption can be reduced with ad additional tuning of the SDRE controller at expenses of larger final errors.

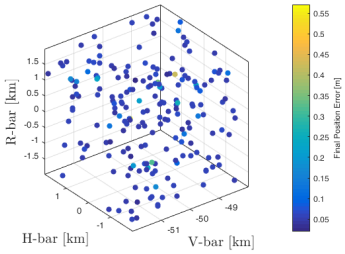

(a) Position Errors

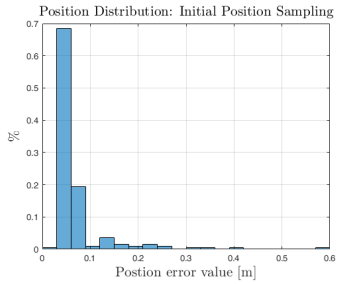

(b) Position Errors distribution

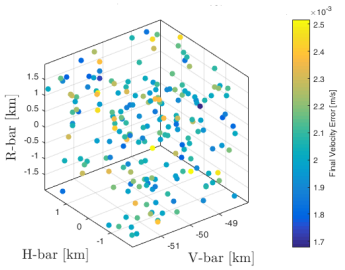

(c) Velocity Errors

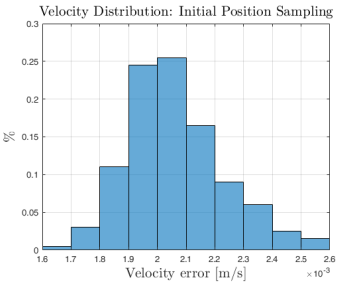

(d) Velocity Errors distribution

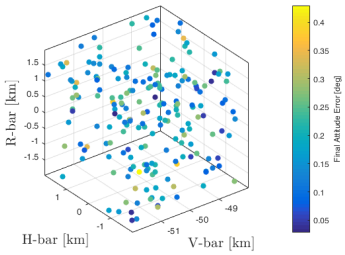

(e) Attitude Errors

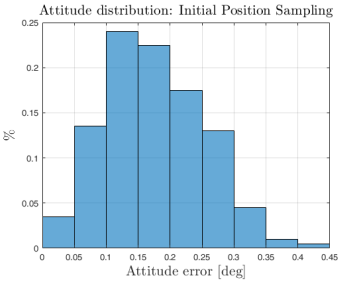

(f) Attitude Errors Distributions

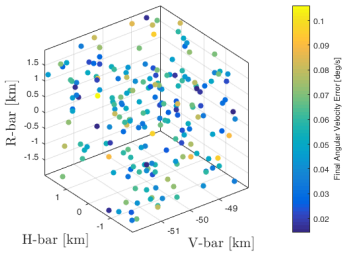

(g) ω Errors

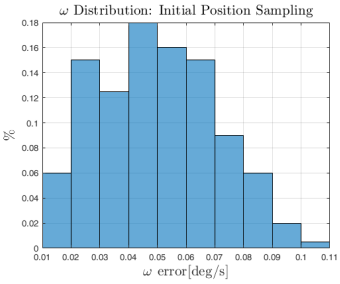

(h) ω Errors Distribution

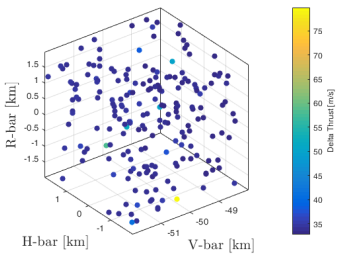

(i) ΔV variation

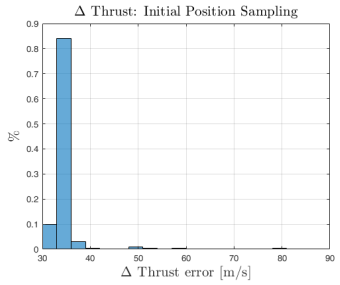

(j) ΔV Variation Distribution

Fig. 13 Position Samples

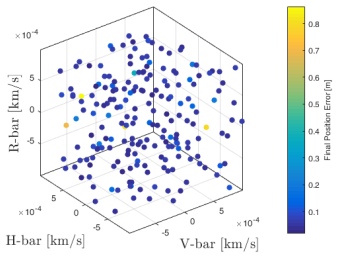

(a) Position Errors

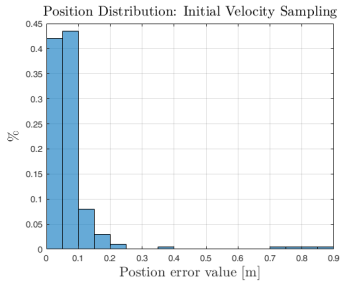

(b) Position Errors distribution

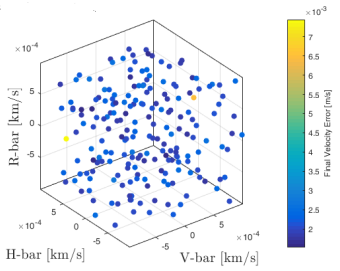

(c) Velocity Errors

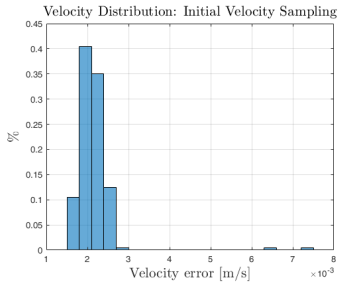

(d) Velocity Errors distribution

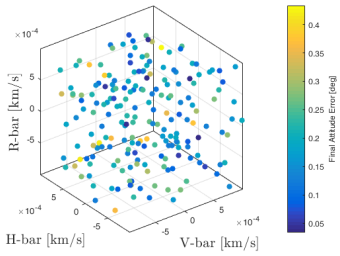

(e) Attitude Errors

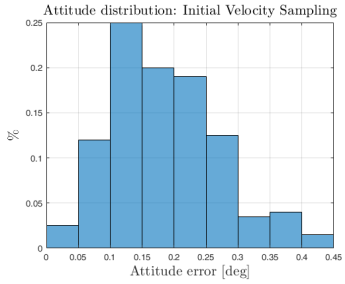

(f) Attitude Errors Distributions

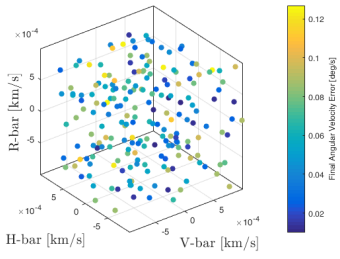

(g) ω Errors

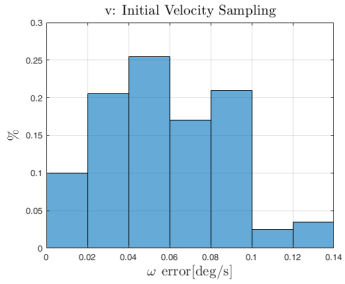

(h) ω Errors Distribution

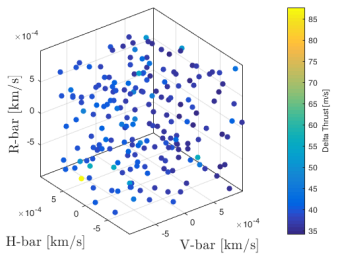

(i) ΔV variation

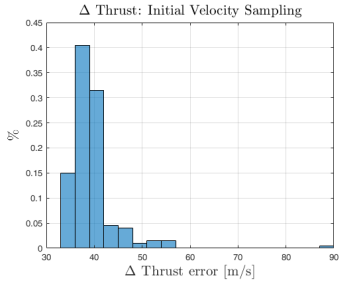

(j) ΔV Variation Distribution

Fig. 14 Velocity Samples

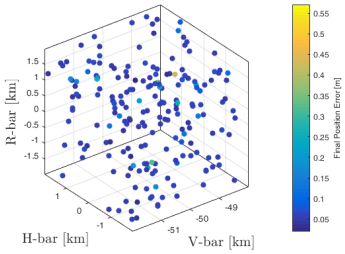

(a) Position Errors

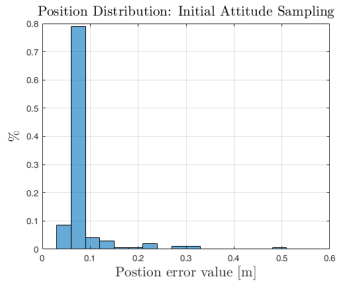

(b) Position Errors distribution

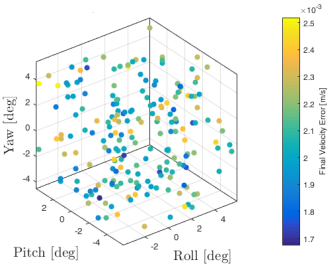

(c) Velocity Errors

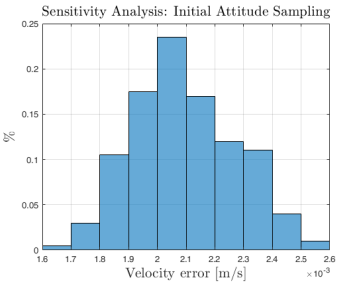

(d) Velocity Errors distribution

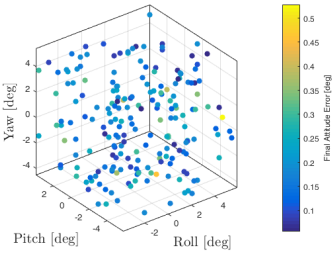

(e) Attitude Errors

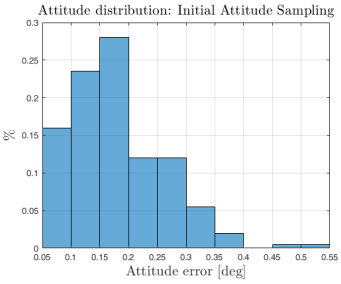

(f) Attitude Errors Distributions

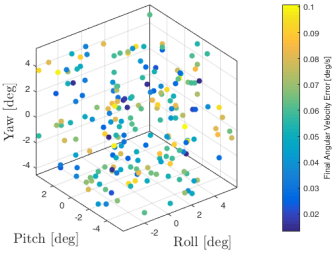

(g) ω Errors

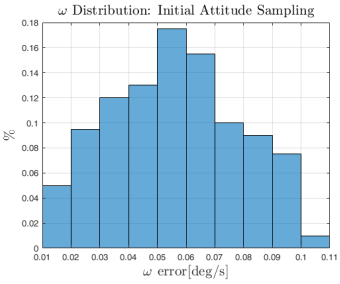

(h) ω Errors Distribution

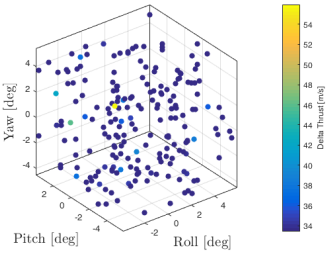

(i) ΔV variation

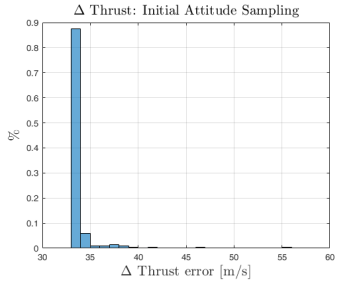

(j) ΔV Variation Distribution

Fig. 15 Attitude Samples

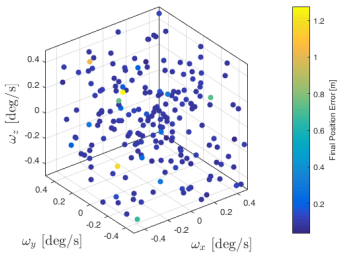

(a) Position Errors

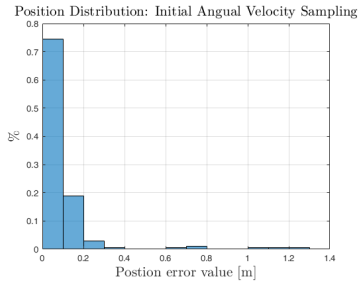

(b) Position Errors distribution

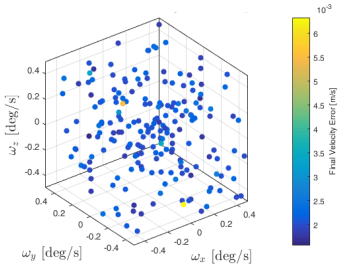

(c) Velocity Errors

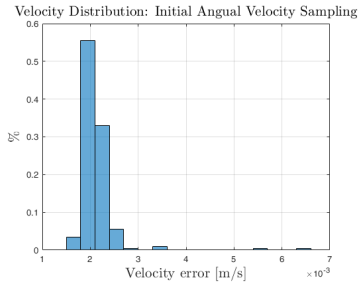

(d) Velocity Errors distribution

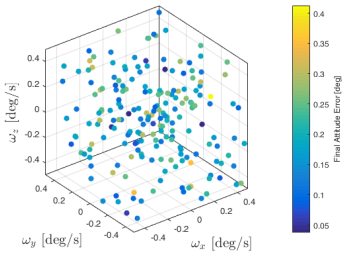

(e) Attitude Errors

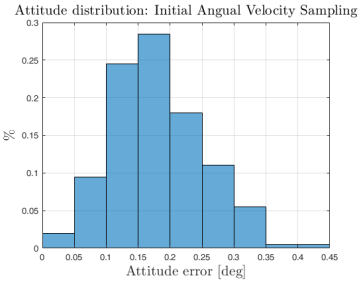

(f) Attitude Errors Distributions

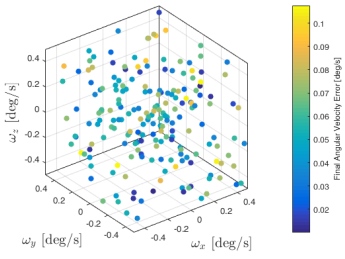

(g) ω Errors

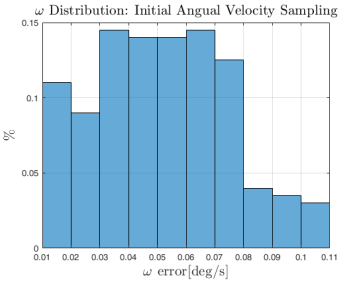

(h) ω Errors Distribution

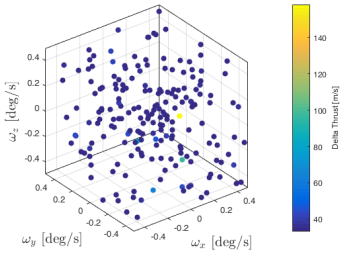

(i) ΔV variation

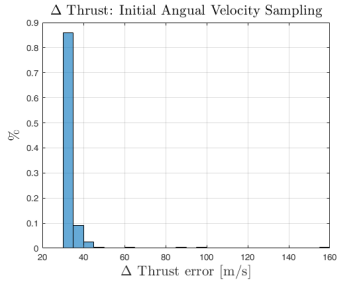

(j) ΔV Variation Distribution

Fig. 16 Angular Velocity Samples

IX. Conclusions

A combined continuous Adjoint guidance and SDRE control were extensively tested under a fairly realistic sensor and actuator models. They were capable of guaranteeing prescribed the safety margins in about the 90% of the tested cases, during a sample rendezvous scenario between two spacecraft under three body gravitation dynamics.
The most appropriate sensor and actuators suite were identified and the detail models of the navigation chain and the actuator were implemented, it was verified that the proposed guidance algorithm was able to guarantee safety margins also in presence of non idealities, and the control allocation structure.

Acknowledgements

This work was partially supported by the European Space Agency under contract No. 000121575/17/NL/hh. The view expressed herein can in no way be taken to reflect the official opinion of the European Space Agency.

References

[1] ISECG, *Global Space Exploration Roadmap*, 2018.

[2] Bucchioni, G., and Innocenti, M., "Dynamical Issues in Rendezvous operations with Third Body Perturbation," ????

[3] Fehse, W., *Automated rendezvous and docking of spacecraft*, Vol. 16, Cambridge university press, 2003.

[4] Ankersen, F., *Guidance, navigation, control and relative dynamics for spacecraft proximity maneuvers*, 2010.

[5] D. C. Woffinden, D. G., "Relative Angles-Only Navigation and Pose Estimation For Autonomous Orbital Rendezvous," *Journal of Guidance, Control and Dynamics*, Vol. 30, 2007.

[6] R. Zanetti, A. S., D. C. Woffinden, "Multiple Event Triggers in Linear Covarience Analysis for Spacecraft Rendezvous," *Journal of Guidance, Control and Dynamics*, Vol. 35, 2012.

[7] ESA, "Lunar Ascent Element, Hunamn Enabled Robotic Architecture and Capabilities for Lunar Exploration and Science, Heracles, framework, ESA-HSO-K-TN-0011," 25/08/2017.

[8] Johansen, T. A., and Fossen, T. I., "Control allocation—a survey," *Automatica*, Vol. 49, No. 5, 2013, pp. 1087–1103.

[9] Jin, J., Park, B., Park, Y., and Tahk, M.-J., "Attitude control of a satellite with redundant thrusters," *Aerospace Science and Technology*, Vol. 10, No. 7, 2006, pp. 644–651.

[10] Boada, J., Prieur, C., Tarbouriech, S., Pittet, C., and Charbonnel, C., "Multi-saturation anti-windup structure for satellite control," *American Control Conference (ACC), 2010*, IEEE, 2010, pp. 5979–5984.

[11] Grechi, S., and Caiti, A., "Comparison between Optimal Control Allocation with Mixed Quadratic & Linear Programming Techniques," *IFAC-PapersOnLine*, Vol. 49, No. 23, 2016, pp. 147–152.

[12] Oppenheimer, M. W., Doman, D. B., and Bolender, M. A., "Control allocation for over-actuated systems," *Control and Automation, 2006. MED'06. 14th Mediterranean Conference on*, IEEE, 2006, pp. 1–6.

[13] Ankersen, F., Wu, S.-F., Aleshin, A., Vankov, A., and Volochinov, V., "Optimization of spacecraft thruster management function," *Journal of guidance, control, and dynamics*, Vol. 28, No. 6, 2005, pp. 1283–1290.

[14] Gurfil, P., Idan, M., and Kasdin, N. J., "Adaptive neural control of deep-space formation flying," *Journal of Guidance, Control, and Dynamics*, Vol. 26, No. 3, 2003, pp. 491–501.

[15] Franzini, G., Innocenti, M., and Casasco, M., "Impulsive Rendezvous Maneuvers in the Restricted Three-Body Problem," ????

[16] Park, H.-E., Park, S.-Y., and Choi, K.-H., "Satellite formation reconfiguration and station-keeping using state-dependent Riccati equation technique," *Aerospace Science and Technology*, Vol. 15, No. 6, 2011, pp. 440–452.

[17] Lefferts, E. J., Markley, F. L., and Shuster, M. D., "Kalman filtering for spacecraft attitude estimation," *Journal of Guidance, Control, and Dynamics*, Vol. 5, No. 5, 1982, pp. 417–429.

[18] Rogers, R. M., *Applied Mathematics in Integrated Navigation Systems, Third edition*, AIAA education series, Blacksburg, Virginia, 2007.

[19] ESA, "Providing Ground Surface system Concept Description Document(CDD)-Robotic Lander," 2017.

[20] Alfriend, K., Vadali, S. R., Gurfil, P., How, J., and Breger, L., *Spacecraft formation flying: Dynamics, control and navigation*, Vol. 2, Elsevier, 2009.

[21] Bucchioni, G., Galullo, M., and Innocenti, M., "Simulation tool for rendezvous and docking in high elliptical orbits with third body perturbation-CCN1: Final Report," ESA Contract No. 4000121575/17/NL/CRS/hh, Pisa, January 24 2019. Issue 1, Revision 3.